

On the nature of the variability of the Martian thermospheric mass density: Results from electron reflectometry with Mars Global Surveyor

Scott L. England¹ and Robert J. Lillis¹

Received 5 October 2011; revised 5 December 2011; accepted 16 December 2011; published 21 February 2012.

[1] Knowledge of Mars' thermospheric mass density is important for understanding the current state and evolution of the Martian atmosphere, and for spacecraft such as the upcoming MAVEN mission that will fly through this region on every orbit. Global-scale atmospheric models have been shown thus far to do an inconsistent job of matching the mass density observations at these altitudes, especially on the nightside. Thus, there is a clear need for a data-driven estimate of the mass density in this region. Given the wide range of conditions and locations over which this must be defined, the data set of thermospheric mass densities derived from energy and angular distributions of super-thermal electrons measured by the MAG/ER experiment on Mars Global Surveyor, spanning 4 full Martian years, is an extremely valuable resource. Here we present an empirical model of the thermospheric density structure of this data set. Using this new model, we assess the global-scale response of the thermosphere to dust storms in the lower atmosphere and show that this varies with both latitude and dust opacity. Further, we examine the short-term variability of the thermospheric density and show that it exhibits a repeatable behavior with latitude and season that is indicative of atmospheric wave activity seen in the lower thermosphere. This short-term variability is consistently highest in the southern hemisphere, peaking around perihelion, which may have significant implications for studies of atmospheric escape.

Citation: England, S. L., and R. J. Lillis (2012), On the nature of the variability of the Martian thermospheric mass density: Results from electron reflectometry with Mars Global Surveyor, *J. Geophys. Res.*, 117, E02008, doi:10.1029/2011JE003998.

1. Introduction

[2] Knowledge of the current state and variability of the Martian thermosphere is vital for understanding both the current evolution of the Martian atmosphere and for spacecraft aerobraking and orbit determination for future missions to Mars such as Mars Atmosphere Volatile Evolution (MAVEN) that will fly through this region on every orbit. Of all the key parameters that define the state of the thermosphere, perhaps the one of greatest import is its density. However, first principles models have thus far had difficulty in reproducing the observed thermospheric density, especially on the nightside [e.g., Lillis *et al.*, 2010], which may be due to the difficulty associated with simulating nightside CO₂ cooling and dynamic processes. Thus, at this time there is a clear need to use observations of the Martian thermospheric density to develop an understanding of the behavior (both the general trends and variability) of this region.

[3] The majority of our knowledge of the density of the Martian thermosphere comes from measurements that do not

distinguish between different chemical species, but rather simply measure the total mass density (ρ hereafter). The bulk of these measurements come from: (1) the accelerometers onboard Mars Global Surveyor (MGS), Mars Odyssey (ODY) and Mars Reconnaissance Orbiter (MRO) [Keating *et al.*, 1998; Tolson *et al.*, 2005, 2008]; (2) Doppler tracking of the MGS and MRO spacecraft [Tracadas *et al.*, 2001; Mazarico *et al.*, 2008; Forbes *et al.*, 2008]; (3) stellar occultations from Mars EXpress (MEX) [Forget *et al.*, 2009; McDunn *et al.*, 2010]; and (4) super-thermal electron pitch angle distributions (PAD hereafter) measured by MGS [Lillis *et al.*, 2005, 2010].

[4] Using the observations described above, some significant discoveries about the overall structure and behavior of the Martian thermosphere have been made. These include the discovery of seasonally dependent meridional density gradients [Withers, 2006], warming of the northern pole during perihelion [Bougher *et al.*, 2006] and strong zonal density variations associated with atmospheric tides [Joshi *et al.*, 2000; Forbes *et al.*, 2002; Wilson, 2002; Withers *et al.*, 2003; Bougher *et al.*, 2004; Angelats i Coll *et al.*, 2004; Mazarico *et al.*, 2008]. In addition, the accelerometer observations described above have been used to study small-scale fluctuations in ρ , believed to be associated with atmospheric gravity waves [Tolson *et al.*, 2007; Creasey *et al.*, 2006a,

¹Space Sciences Laboratory, University of California, Berkeley, California, USA.

2006b; Withers, 2006; Wang *et al.*, 2006; Fritts *et al.*, 2006; Forbes *et al.*, 2006].

[5] Significant discoveries have been made using each of the techniques listed above, but only the PAD measurements from MGS have measured ρ thus far in the nightside thermosphere over a wide range of both locations and solar and atmospheric conditions. Thus, with the aim of investigating and attempting to define the behavior of ρ one of the regions that MAVEN will encounter, the present work will focus on using these data. The determination of ρ from the PAD measurements of MGS have been discussed in detail by Lillis *et al.* [2005], Lillis *et al.* [2008b] and Lillis *et al.* [2010]. Briefly, the technique makes use of the asymmetries in the pitch angle distributions of the upgoing and down-going super-thermal electron populations and measured magnetic field by MGS at its orbital altitude of $\sim 370\text{--}430$ km to infer information about both the magnetic field and ρ of the upper thermosphere in the region around 185 km altitude (ρ_{185} hereafter). Initial estimates of altitude profiles of relative atmospheric composition and ρ are required for this technique and have previously been supplied by the Mars Thermosphere General Circulation Model (MTGCM hereafter), which is now coupled to the NASA AMES Mars General Circulation Model (MGCM hereafter) (e.g. Bougher *et al.* [2004, 2006]).

[6] Using the PADs, Lillis *et al.* [2010] presented an analysis of ρ_{185} based on four Martian years of observations from MGS. The authors showed that ρ_{185} : (1) responds globally to Mars' heliocentric distance; (2) displays strong inter-hemispheric/seasonal variations such as the difference in the density of the aphelion winter hemisphere to the perihelion winter hemisphere; and (3) shows a broad low density in the southern hemisphere winter near aphelion and that shifts progressively later with respect to the Martian seasons as the solar cycle progresses from solar maximum to solar minimum, although dust loading may also play a part in this variation.

[7] Here we use the same large database (~ 1 million data-points covering a wide range of locations and conditions) from Lillis *et al.* [2010] (section 2) to develop a new empirical model which describes the spatial, seasonal and solar-flux induced variability of ρ in the upper thermosphere (section 4). Using this model of the long-term and large-scale variability of ρ , we are then able to perform the first ever characterization of the temporal and spatial patterns in the short-term and small-scale variability from the PAD-inferred values of ρ (section 5). Knowledge of both the mean and variations in ρ are important for upcoming missions such as MAVEN.

2. The MGS MAG-ER Observations

[8] As the range of conditions for which observations exist is so vital for the development of any empirical model, this section will provide a description of the availability of the data that will be used in this study. Section 2.1 will describe the availability of the individual PAD observations from MGS. Each of these PADs is used to produce an estimate of the atmospheric density profile, but only some subset of these are of high quality. The selection of these high quality profiles is described in section 2.2.

2.1. Availability of PAD Observations

[9] Figure 1a shows the distribution of observations over the surface of Mars that will be used in this study. Neutral density probing with electron reflectometry (ER hereafter) requires crustal magnetic field strengths of at least 15 nT at 185 km [Lillis *et al.*, 2010] and magnetic field lines that are open to the solar wind. Given that open field lines are much more common on the night side [Brain *et al.*, 2007] the distribution of available data bears resemblance to the nightside 'open' topology maps shown by [Brain *et al.*, 2007] and [Lillis *et al.*, 2008a]. That is, the data is concentrated in bands where the crustal magnetic field is mostly vertical. Most notably, data are absent over large areas of the planet where the crust is weakly magnetized if at all: the volcanic Tharsis province ($\sim 0^\circ\text{--}90^\circ\text{N}$, $\sim 220\text{--}300^\circ\text{E}$) [Lillis *et al.*, 2009] and the giant impact basins Hellas ($\sim 45^\circ\text{S}$, 75°E), Utopia ($\sim 45^\circ\text{N}$, 120°E) and Argyre ($\sim 60^\circ\text{S}$, 285°E) [Lillis *et al.*, 2008a]. The result is that large parts of the northern hemisphere and moderate parts of the southern hemisphere are not sampled in our data set. This areographic distribution of the data has important consequences for the strengths and limitations of the present work. The strengths include: data exist at all latitudes and all values of solar longitude (not shown here), allowing for the empirical model to be fully constrained with respect to seasonal variations that change as a function of latitude; data are available at all longitudes, which is required to find the zonal mean density in the presence of strong non-migrating atmospheric tides that are known to exist in the Martian thermosphere (see section 1); the same locations are sampled repeatedly, allowing for inter-annual variability to be characterized well, including the effects of dust-storms. The main weakness is that not all longitudes are sampled at each latitude, especially in the northern hemisphere, which has implications for our ability to describe longitudinal density variations such as those associated with non-migrating atmospheric tides.

[10] Figure 1b shows the distribution of available observations with respect to solar F10.7 flux (scaled and rotated appropriately from Earth to give an estimate for Mars) and time over the ~ 4 Martian years for which the MGS data are available. The effect of Mars' heliocentric distance is apparent, along with the solar cycle. The PAD observations are available from close to solar maximum in Mars Year 25 to close to solar minimum in Mars Year 27. Thus, the empirical model can be constrained by data at all typical solar flux levels (the main exceptions being the lack of data at extremely high solar flux levels associated with flares and the extremely low solar flux levels that were seen during the most recent solar minimum around 2008–2009).

[11] Perhaps the largest deficiency in the present data set is the coverage in local time (LT hereafter). MGS is in a quasi sun-synchronous orbit, with the best sampling around 2am and 2pm LT at low- to midlatitudes. Wide LT sampling is only available in the polar regions. This will require careful consideration when examining the effects of LT on ρ (section 3.3). Further, it can be expected that with only 2 samples ~ 12 hours LT apart, our analysis will be unable to reveal the effects of semi-diurnal tides on ρ . Any migrating semi-diurnal tides present at low–midlatitudes will be manifest as an offset in the mean value of ρ at these latitudes, while any non-migrating semi-diurnal tides present will

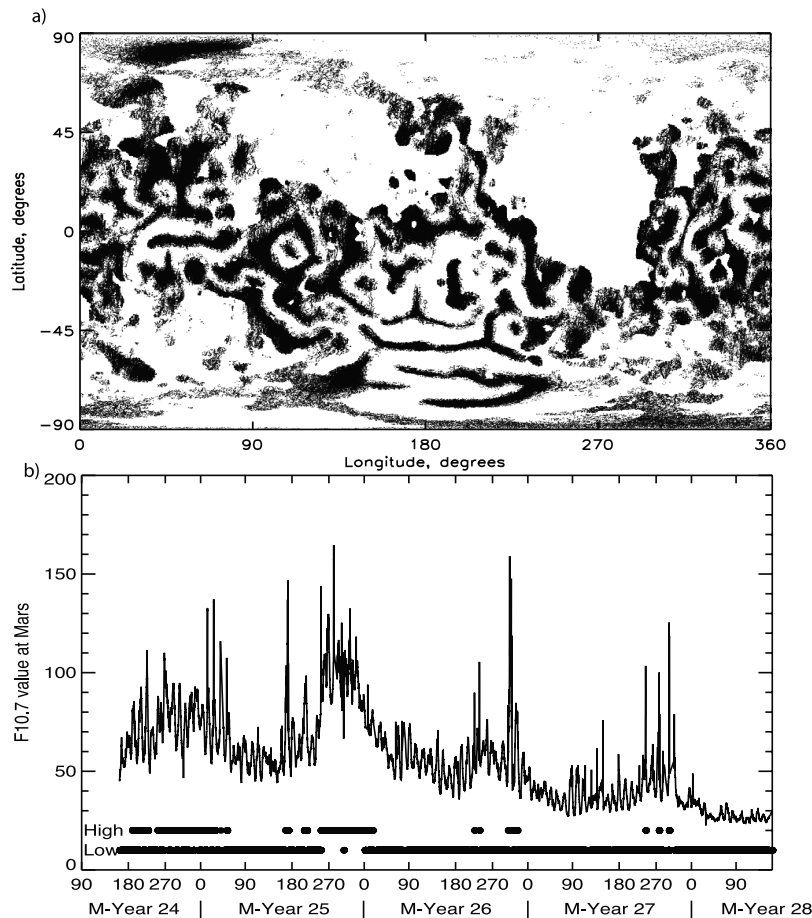


Figure 1. (a) Areographical distribution of the observations available for this study. Each black dot marks the location of one datum. (b) Distribution of the observations as a function of time and F10.7 index value at Mars. Observations are separated into high and low solar flux (above and below F10.7 of 80) as described in the text. The distribution of these two populations with time throughout the data set is shown by the black dots at the bottom of the plot.

appear as longitudinally stationary structures. More consideration of atmospheric tides is given in section 5.

2.2. Selection of Atmospheric Density Profiles

[12] The ER technique searches for the profile of electron-neutral scattering probability versus altitude that provides the best-fit to the PAD observed by MGS. To perform such a fit, knowledge of the atmospheric composition as a function of altitude, along with the scattering cross-section for each of those chemical species, is required. A profile of the composition and an initial estimate of the atmospheric density is provided by the MTGCM. The MTGCM is a primitive equation model that solves for time-dependent neutral temperatures, neutral and ion densities, and neutral winds over the globe [Bougher *et al.*, 2004, 2006]. The MTGCM simulates these fields on 33 pressure levels, corresponding to ~ 70 – 300 km ($1/2$ scale-height resolution) with $5^\circ \times 5^\circ$ horizontal resolution. At its lower boundary, the model is coupled to the MGCM [Haberle *et al.*, 1999], which allows the effects that couple the lower and upper atmosphere, such as the upward propagation of atmospheric tides and thermal expansion of the lower atmosphere during dust storms [Bougher *et al.*, 2004, 2006; McDunn *et al.*, 2010], to be

represented well in the MTGCM. The MTGCM code has been updated to include a non-local thermodynamic equilibrium $15\text{-}\mu\text{m}$ CO_2 cooling scheme along with the corresponding near-infra-red heating rates [López-Valverde *et al.*, 1998; Bougher *et al.*, 2006]. Taking key input factors such as the solar UV flux (F10.7 and E10.7 indices), heliocentric distance and solar longitude, the MTGCM provides altitudes profiles of the major neutral species, selected minor neutral species and photochemical ions species. Figure 2 shows an example of such a profile from the MTGCM model for 2 am equatorial, equinox and moderate solar flux conditions (F10.7 of 50 at Mars). As the scale height of each species is different at thermospheric altitudes, individual profiles for each species such as those shown here must be used. The ER technique of Lillis *et al.* [2010] finds (by fitting to the measured PADs) the scaling factor to apply to this density profile, i.e. a scaling factor of 10 means that a density profile 10 times higher than our initial guess provides the best fit. Lillis *et al.* [2008b] showed that the technique is most sensitive to the values of ρ around 185 km and is approximately constrained over 1 scale height above and below this level. Thus, throughout we shall refer to the data found as ρ_{185} .

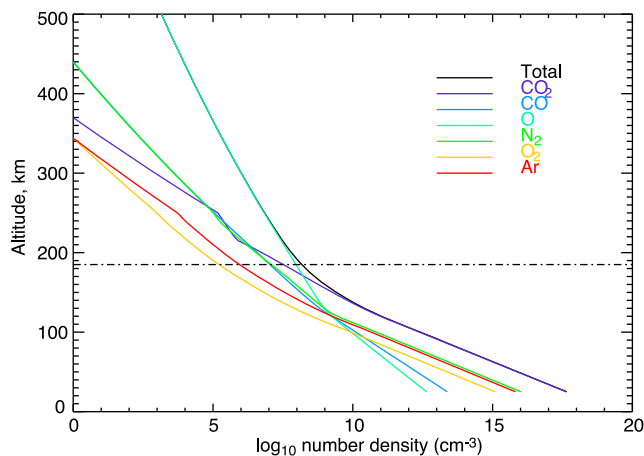


Figure 2. Reference altitude profiles of the number densities of each of the major species in the Martian thermosphere from the MTGCM that are used in the determination of the mass densities from the MGS MAG-ER. Profiles for each individual chemical species are used to define the a priori scattering cross-sections as a function of altitude as described in the text. Values shown here are for solar-moderate conditions. The altitude of maximum sensitivity of the MGS MAG-ER results is marked by the horizontal dot-dash line.

[13] *Lillis et al.* [2010] provided a detailed account of the sources of error in fitting the MGS data to the kind of atmospheric composition profile shown in Figure 2. Their analysis revealed that their technique is less reliable (as defined by the standard deviation of retrieved profiles for the same conditions) when the magnetic field is particularly weak (less than 15 nT at 185 km), the magnetic field geometry at MGS was unfavorable (the absolute elevation angle of the magnetic field was less than 40°) or when MGS was in sunlight (the solar zenith angle was less than 113°). Accordingly, the authors discarded these data from their analysis. As we wish to use the maximum amount of high quality data to constrain the empirical model developed here, we will adopt these same criteria for data selection with regard to the magnetic field. However, in order to construct our empirical model, we do not wish to discard all of the data from the dayside and thus it is worth discussing both the potential implications of including these data on our model and our strategy to assess and mitigate these effects. *Lillis et al.* [2010] argued that the primary sources of the decreased reliability of their technique on the dayside where: 1) the solar wind contribution to the total magnetic field at the MGS satellite tends to be stronger on the dayside, which often results in both a more horizontal magnetic field seen by MGS (lower magnetic elevation angle) and makes the mapping of the magnetic field down to an altitude of 185 km less reliable; 2) fewer open magnetic fields with associated loss cones were observed on the dayside, resulting in fewer estimates of ρ_{185} and thus making it more difficult to constrain ρ_{185} as accurately; 3) the electron-pitch angle observations on the dayside (on which the ER technique is based) are potentially contaminated by photoelectrons; and 4) the electron-pitch angle observations on the dayside are additionally contaminated by electrons produced from soft X-rays in the

~ 500 eV range [*Mitchell et al.*, 2000]. Our selection criterion for the magnetic field elevation angle eliminates the close-to-horizontal magnetic field cases from our study. Further, we have introduced an additional selection criterion to mitigate the profiles for which the magnetic field is poorly constrained. Each fitted ρ profile has an associated χ^2 value that describes the goodness of the fit of the modeled PAD to that observed by MGS. Here we discard all data for which the reduced χ^2 value is 3 or greater. These two criteria essentially eliminate the contribution of factor 1) to our model. While factor 2) limited the usefulness of the dayside data for the study by *Lillis et al.* [2010], there does appear to be sufficient data on the dayside ($\sim 200,000$ samples) to constrain the empirical model in this region. *Fox and Dalgarno* [1979] and *Liemohn et al.* [2006] have shown that most photoelectrons produced at Mars are in the energy range below 60 eV, and thus would not be detected by the MAG instrument. Therefore we suggest here that factor 3) listed above should not play a major part in contaminating the dayside data. However, as electrons of energy ~ 500 eV would be detected by the MAG instrument, factor 4) must be considered carefully. Our use of the χ^2 value criterion will remove the cases where soft X-rays severely contaminate the electron-pitch angle observations from our database. For the more moderate cases that are not excluded, this factor likely contributes to an increased uncertainty in the dayside data that we will use in this study. In section 5.1, we will explore the impact of including these dayside data on the variability of ρ_{185} observed (which is a sum of both natural variability and any artifacts of the measurement technique).

[14] Using both the magnetic field and χ^2 selection criteria described above, we have ~ 1 million ‘good’ data points that will be used in this study. The distribution of these is shown in Figure 1.

[15] Finally, it should be noted here that all data taken during the planet-wide dust storm of Mars Year 25, when the observed values of ρ_{185} were far from typical, will be excluded when formulating our initial empirical model. By comparing our initial empirical model to these data afterwards, we will be able to establish in detail the impact of this dust storm on ρ_{185} and characterize this in the final empirical model (see section 3.4).

3. Trends in the Value of ρ_{185}

[16] This section describes the steps by which the trends in the observed values of ρ_{185} are found and thus how the empirical model is made. As a result of the combination of both uneven or sparse data sampling in certain locations and a relatively high level of variability in each individual sample (as a result of both the very large natural variability of ρ_{185} and the uncertainties inherent in the ER technique), it is not possible to simply assume a functional form of ρ_{185} and then perform a single least squares fit to the entire data set. Instead, the trends in ρ_{185} with respect to one or two variables at a time are found and the fits to these parameters are used to successively de-trend the values of ρ_{185} . The choice of the order and scope of each of these de-trending steps is therefore important and should be made carefully. It should therefore be noted here that a number of different permutations of the de-trending steps have been made and what is

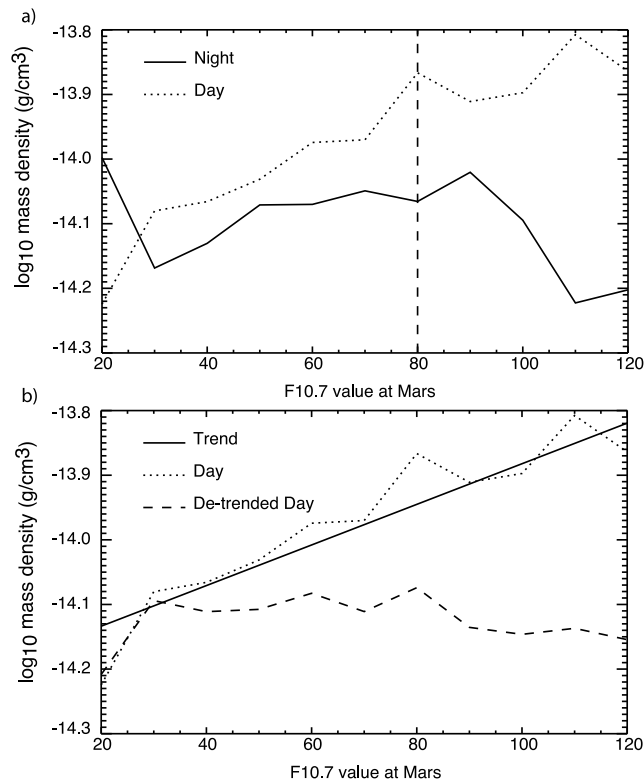


Figure 3. (a) Global mean mass density at 185 km altitude as a function of F10.7 index value. Values during daylight (solar zenith angle less than 113°) are shown by the dotted line and values during shadow (solar zenith angle greater than 113°) are shown by the solid line. The divide between the solar minimum and maximum reference profiles is marked by the vertical dashed line. (b) Daylight values from Figure 3a are shown by the dotted line. The linear fit to this trend is shown by the solid line. After this trend is removed, the daylight values have no clear trend with F10.7 index, as shown by the dashed line.

presented here is the method that achieved the best overall fit to the data.

3.1. The Trend With Solar UV Flux

[17] The first trend to be found is the response of ρ_{185} to solar flux. The F10.7 index is a widely used proxy for the solar UV flux at the orbit of Earth. In the absence of a measured solar UV flux at Mars during the MGS mission, the F10.7 index is used as the basis for our solar UV proxy at Mars. To account for the differing distance to the sun from Earth and Mars, the F10.7 values are adjusted using the relative heliocentric distances of the two planets. To account for the relative location of the planets in solar longitude, a time series of F10.7 value at Earth are shifted and interpolated in time to match the solar longitude of Mars using the assumption that the sun rotates as a solid body with a period of 27 Earth days.

[18] Figure 3a shows the mean dayside and nightside (where day and night are defined by a solar zenith angle below and above 113° respectively) value of ρ_{185} as a function of F10.7 at Mars. An increase in ρ_{185} with F10.7 is evident for the dayside values, but no clear trend is seen for

the nightside values. This appears to indicate that the dayside thermosphere responds more directly to changes in the UV flux and possibly that other processes are more important in determining the nightside thermospheric density [e.g., Bougher *et al.*, 2006; Lillis *et al.*, 2010].

[19] As mentioned earlier, the ER technique requires an altitude profile of the main chemical species in the thermosphere (Figure 2) as an input. As this profile changes with the level of solar UV flux and our data cover a wide range of solar flux levels from solar maximum to minimum, a single input profile is likely not a valid initial guess for all of these cases. Rather, two profiles are selected, one for relatively high solar activity (F10.7 of ~ 90 at Mars) and one for relatively low solar activity (F10.7 of ~ 50 at Mars). The ER technique switches between these 2 input profiles at a value of F10.7 of 80 (shown by the dashed line in Figure 3a). This value was determined by testing all possible transitions between the ‘high’ and ‘low’ input profiles to find when the difference in the retrieved value of ρ_{185} using each was minimized. It can be noted here that none of these values of the transition significantly altered the result for the nightside trend shown here.

[20] Figure 3b repeats the mean dayside value of ρ_{185} as a function of F10.7 from Figure 3a (dotted line) and shows the least squares fit to this trend (solid line). This function is then used to de-trend all dayside values of ρ_{185} . The de-trended values (dashed line) shows no clear trend with F10.7. These de-trended values are used in the subsequent analyses described in sections 3.2–3.4.

3.2. The Trend With Solar Longitude and Areographic Latitude

[21] As a result of Mars’ orbital obliquity ($\sim 25^\circ$), it can be expected that the trend in ρ_{185} with solar longitude cannot adequately be captured by considering a global-mean value of ρ_{185} . Yet, given that Mars’ orbital eccentricity is so large (~ 0.095), it can also be expected that the variation in ρ_{185} with solar longitude may not be simply antisymmetric about the equator. Therefore, a fit of ρ_{185} to both solar longitude and areographic latitude must be performed simultaneously.

[22] The fit is performed in two steps. First, the data are separated into six latitudinal bins, each 30° wide. For each of these bins, the combined mean, annual and semi-annual trend in ρ_{185} is found. In the second step, the coefficients that define each of the six fits from step one are fitted for linear, symmetric and anti-symmetric functions in latitude. This results in a function that is smooth and continuous across all values of solar longitude and areographic latitude.

[23] Figure 4a shows the values of ρ_{185} as a function of solar longitude and areographic latitude. This can be compared with Figure 4b, which shows the smooth function described above. The function captures the main global-seasonal trends in ρ_{185} quite well. Following the same process described in section 3.1, this function is used to de-trend the values of ρ_{185} that are used in sections 3.3 and 3.4.

3.3. The Trend With Local Time and Latitude

[24] In a similar manner to the trend with solar longitude, from purely geometric considerations it may be expected that the trend in ρ_{185} with LT would be a function of latitude. While the polar regions at 185 km altitude are often in continuous sunlight or shadow, the equatorial regions

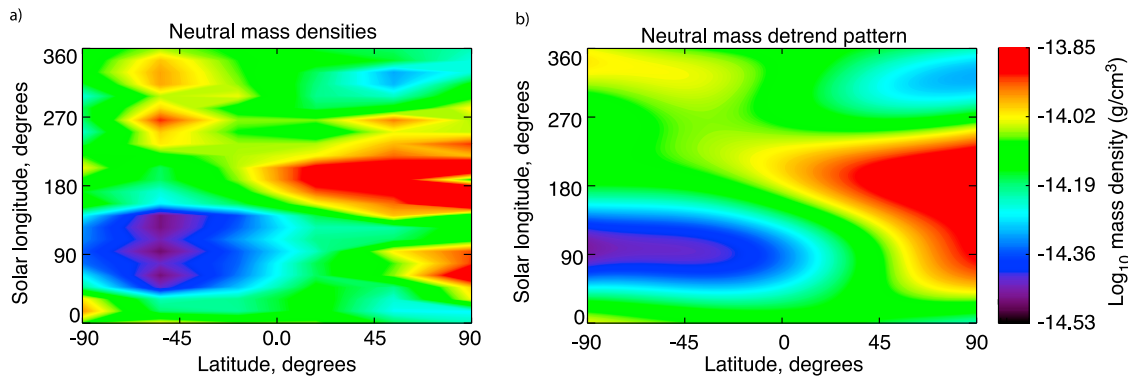


Figure 4. (a) Zonal-diurnal mean mass density at 185 km as a function of solar longitude and areographical latitude from the MGS MAG-ER observations. (b) Reconstruction of the annual and semi-annual trends as a function of areographical latitude. These functions are used to de-trend the data as described in the text.

experience approximately equal amounts of day and night throughout the year.

[25] The challenge in finding the trend in ρ_{185} with LT in the MGS data relates to the distribution of the PAD observations as stated in section 2.1. Figure 5a shows the distribution of the available observations as a function of LT and latitude. With the exception of the polar regions, essentially all of the available data cover just two LTs (one close to 2 and one close to 14 LT). In the absence of any other data to help constrain the behavior of ρ_{185} in-between these two LTs, only the diurnal cycle in ρ_{185} can be found; there is simply no information regarding the semi-diurnal cycle in the MGS PAD data across most of the planet. Further, there is insufficient information to define the phase of the diurnal cycle

(the LT of the peak value in ρ_{185}) beyond demonstrating that is closer to 2 or 14 LT. A simple analysis of the values of ρ_{185} reveals that they are consistently higher at 14 LT than 2 LT and, as will be shown in section 4, arbitrarily choosing the phase to be 14 LT produces results that are in good overall agreement with previous studies of the thermospheric density at similar altitudes, so this lack of information is not critical in the development of the empirical model. Further, there is ample information regarding the behavior of ρ_{185} as a function of latitude that will enable a fit to be performed in both LT and latitude simultaneously.

[26] Following the approach described in section 3.2, the values of ρ_{185} are divided into 6 bins in latitude. For each bin, the mean value and amplitude of the diurnal cycle are

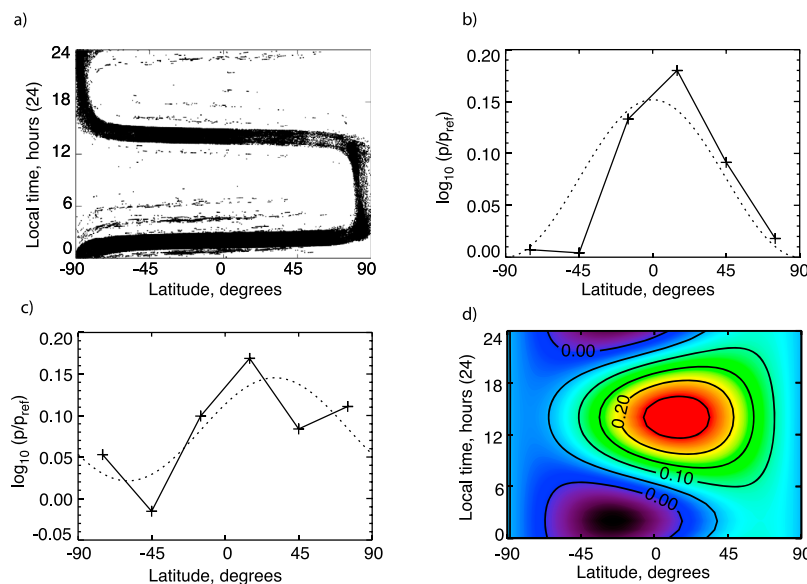


Figure 5. (a) Distribution of the data available for this study as a function of local time (in Martian hours) and areographical latitude. Each black dot represents one datum. (b) Global symmetric trend in diurnal cycle of mass densities at 185 km. Zonal mean observed values are shown by the solid line and plus symbols. Least squares fit to these data is shown by the dotted line. (c) As Figure 5b but for the global asymmetric mode. (d) Reconstruction of the local time-latitude trend in the mass densities at 185 km. This trend is removed from the data as described in the text.

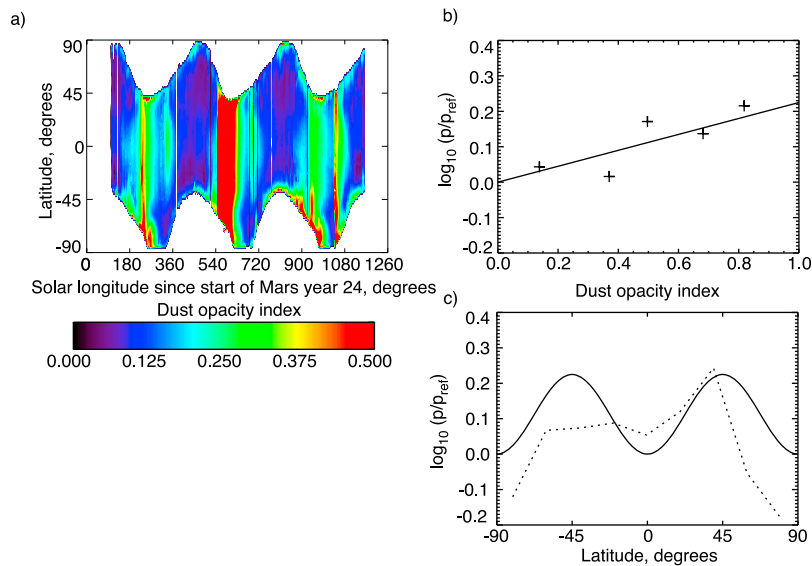


Figure 6. (a) Mean dayside dust opacity index from MGS-TES [Smith, 2004] as a function of areographical latitude and cumulative solar longitude since the start of Mars year 24. These indices are only available through Mars year 26, so only these data are used in determining the trend with dust opacity. (b) Global mean mass density at 185 km as a function of dust opacity index, compared to the reference density value (Figure 2). The observations are shown by the plus symbols. The least squares fit to these data is shown by the solid line. (c) As Figure 6b, but for the areographical latitudinal variation in the trend with dust opacity index.

found. These are shown by the solid lines in Figures 5b and 5c respectively. The mean values are fit with a symmetric and anti-symmetric function in latitude, shown by the dotted line in Figure 5b. The diurnal cycle amplitudes are fit with a latitudinally-symmetric function, shown by the dotted line in Figure 5c. These two functions combined define the mean and diurnal cycle in ρ_{185} shown in Figure 5d. This function is used to de-trend the values of ρ_{185} that are used in the following section.

3.4. The Trend With Dust Opacity and Latitude

[27] Thus-far, the values of ρ_{185} have been de-trended for solar longitude, areographic latitude, LT and solar UV flux level. The main trend left to consider is the change in ρ_{185} during lower-atmosphere dust-storms. The analysis presented in sections 3.1–3.3 excluded the values of ρ_{185} observed during the major dust-storm of Mars Year 25, but all values were de-trended in the same manner. In order to quantify the impacts of a range of dust-storms from minor to major, all data are now used.

[28] To quantify the level of lower-atmospheric dust activity associated with each value of ρ_{185} , the dust opacity values from the MGS-TES instrument are used [Smith, 2004]. These values are shown in Figure 6a as a function of areographic latitude and cumulative solar longitude since the start of Mars Year 24. The MGS-TES data are only available through Mars Year 26, so only data up to this point are considered here. As dust opacities are not always available at the same latitude as the PAD observations each day, and the dust opacity values are only measured on the dayside whereas PAD observations are made both day and night, the global-mean dayside dust opacities for each day are used. The assumption of such a planetary-scale response to even

regional dust-storms can be justified at thermospheric altitudes as the atmospheric temperature has been seen to increase across both hemispheres at thermospheric altitudes during such events [Conrath et al., 2000]. Correspondingly, thermospheric mass densities at 130 km have also been observed to increase in the opposite hemisphere from the onset of a regional storm after a few days [Keating et al., 1998].

[29] Previous studies have shown a significant increase of the thermospheric mass density during lower-atmosphere dust-storms [Keating et al., 1998; Bougher et al., 1999; Bruinsma and Lemoine, 2002; Fritts et al., 2006; Tolson et al., 2007; Mazarico et al., 2008; Forget et al., 2009; Lillis et al., 2010; McDunn et al., 2010]. To find the response of the de-trended values of ρ_{185} , these data are sorted into 5 bins, each spanning a range of dust opacity index of 0.2. The change in ρ_{185} with dust opacity is shown in Figure 6b, where the plus symbol shows the mean value of dust opacity and ρ_{185} in each bin. The solid line shows the least squares fit to this trend, which shows the global-scale increase in ρ_{185} with increasing dust opacity.

[30] To investigate if this response is the same at all latitudes, the data are divided into 9 bins of 20° each. For each of these bins, a similar least squares fit to that shown in Figure 6b is performed. Figure 6c shows the amplitude of each of these fits (the change in ρ_{185} as the dust opacity changes from 0 to 1) as a function of latitude (dotted line). This reveals a latitudinal trend that appears to peak at midlatitudes and minimize around the equator and in the polar regions. The solid line in Figure 6c shows a symmetric function that is fit to these points. This latitudinal fit, along with the increase shown in Figure 6b define the change in ρ_{185} with dust opacity. This defines the final input to the behavior of ρ_{185} that will be

Table 1. Numerical Values of the Coefficients in Equation (1) (All Dimensionless)

| Coefficient | Value | Coefficient | Value |
|-------------|------------------------|-------------|------------------------|
| a_1 | 3.14×10^{-3} | a_2 | -14.1 |
| a_3 | 9.60×10^{-4} | a_4 | 5.77×10^{-3} |
| a_5 | -1.91×10^{-2} | a_6 | -7.14×10^{-2} |
| a_7 | 1.45×10^{-3} | a_8 | 4.35×10^{-2} |
| a_9 | -4.85×10^{-2} | a_{10} | -5.26×10^{-2} |
| a_{11} | -1.39×10^{-3} | a_{12} | -2.02×10^{-2} |
| a_{13} | 9.90×10^{-3} | a_{14} | 2.72×10^{-2} |
| a_{15} | 3.58×10^{-4} | a_{16} | 6.50×10^{-3} |
| a_{17} | -1.39×10^{-2} | a_{18} | 5.87×10^{-2} |
| a_{19} | -6.03×10^{-4} | a_{20} | 1.70×10^{-2} |
| a_{21} | 1.31×10^{-2} | a_{22} | 8.34×10^{-2} |
| a_{23} | 5.43×10^{-2} | a_{24} | 3.01×10^{-2} |
| a_{25} | -1.52×10^{-1} | a_{26} | 3.66 |
| a_{27} | 1.17×10^{-1} | | |

represented in the empirical model. The following section will summarize this model.

4. The Empirical Model

[31] Using the fits from section 3, the $\log_{10}(\rho)$ (in g cm^{-3}) is given by

$$\begin{aligned}
 \text{Solar flux} & \Delta a_1 (F_{10.7} - 60) / [(1.52 + 0.14 \cos(L_s - 71))^2] \\
 \text{Global} & + a_2 + a_3 \theta + a_4 \sin(2\theta) + a_5 \cos(2\theta) \\
 \text{Annual} & + [a_6 + a_7 \theta + a_8 \sin(2\theta) + a_9 \cos(2\theta)] \sin(L_s) \\
 & + [a_{10} + a_{11} \theta + a_{12} \sin(2\theta) + a_{13} \cos(2\theta)] \cos(L_s) \\
 \text{Semiannual} & + [a_{14} + a_{15} \theta + a_{16} \sin(2\theta) + a_{17} \cos(2\theta)] \sin(2L_s) \\
 & + [a_{18} + a_{19} \theta + a_{20} \sin(2\theta) + a_{21} \cos(2\theta)] \cos(2L_s) \\
 \text{Latitudinal} & + [a_{22} + a_{23} \sin(2\theta) + a_{24} \cos(2\theta)] \\
 \text{Local time} & + [a_{25} \cos^2(\theta) \cos(2\pi(LT - 14)/24)] \\
 \text{Dust opacity} & + a_{26} D [a_{27} \sin^2(2\theta)], \quad (1)
 \end{aligned}$$

where Δ is equal to 0 for solar zenith angles greater than 113° and 1 for all other angles, $F_{10.7}$ is the solar 10.7 cm flux measured at Earth, adjusted for the relative solar longitudes of Earth and Mars, in $\text{Js}^{-1}\text{m}^{-2}\text{Hz}^{-1}$, θ is the areographic latitude in degrees, L_s is the solar longitude in degrees, LT is the local time in Martian hours and D is the average dayside dust opacity index (a value from 0–1). The coefficients a_1 through a_{29} are given in Table 1. The terms labeled ‘Solar flux’ come from the trend with solar UV flux described in section 3.1, the ‘Global’, ‘Annual’ and ‘Semi-Annual’ terms come from the trend with solar longitude and areographic latitude described in section 3.2, the ‘Latitudinal’ and ‘Local time’ terms come from the trend with latitude and local time described in section 3.3 and the ‘Dust opacity’ terms come from the trend with lower-atmospheric dust opacity described in section 3.4. A tool for solving equation (1) given any input areographic location, solar $F_{10.7}$ index, solar longitude and dust opacity can be found <http://sprg.ssl.berkeley.edu/~england/>.

[32] The behavior of the atmospheric mass density as defined by equation (1) can now be examined. Figure 7 shows three examples of the values from equation (1) as functions of (a) latitude and LT, (b) areographic latitude and

solar longitude and (c) dustopacity and latitude. Noting the discrepancies in altitude (185 km versus 150 km) and values plotted (CO_2 mass density and total mass density), Figure 7a can be qualitatively compared with the output from the DTM-Mars [Bruinsma and Lemoine, 2002] and Mars-GRAM 2000 [Justus and James, 2000] models (see Figure 8 of Bruinsma and Lemoine [2002]). All three model outputs represent the same solar longitude and solar flux conditions. Comparing the LT of the peak density, equation (1) predicts this to occur around 14 LT whereas both the DTM-Mars and Mars-GRAM 2000 models show this to be around 16 LT. Given that the MGS PAD data was unable to define this more accurately than to within the nearest 12 hours LT, this correspondence is remarkably good and demonstrates that the lack of LT coverage in the input data has not severely impacted the validity of the empirical model produced. Comparing the latitudinal and LT gradients away from the

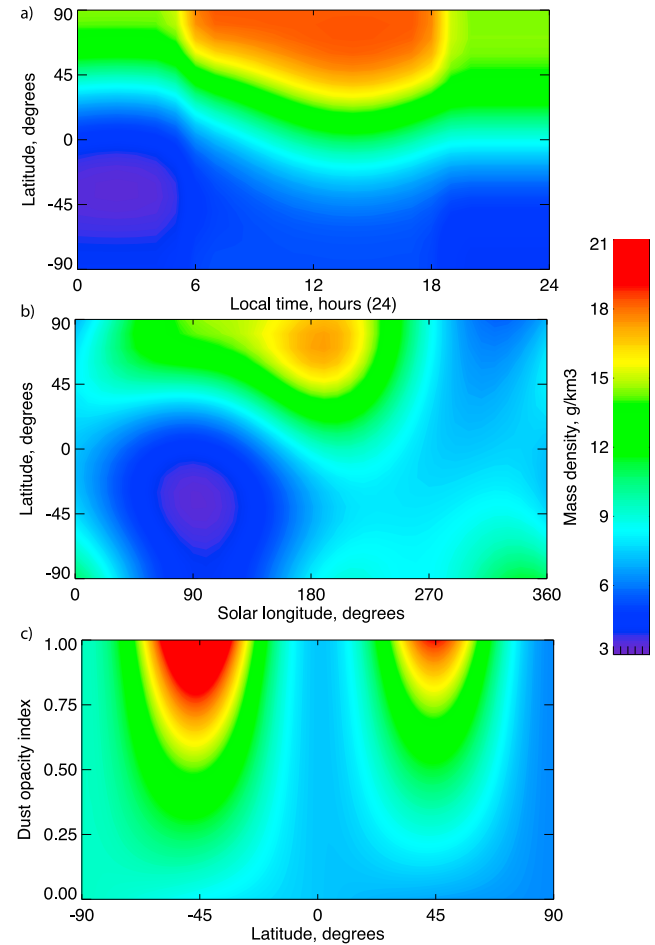


Figure 7. Mass densities from the empirical model as functions of (a) areographical latitude and local time in Martian hours at 185 km altitude, $F_{10.7} = 150 \text{ Js}^{-1}\text{m}^{-2}\text{Hz}^{-1}$ at Earth, dust opacity = 0 and solar longitude = 90° ; (b) areographical latitude and solar longitude at 185 km altitude, $F_{10.7} = 180 \text{ Js}^{-1}\text{m}^{-2}\text{Hz}^{-1}$ at Earth, dust opacity = 0 and local time = 1 (Martian hours); (c) dust opacity index and areographical latitude at 185 km altitude, $F_{10.7} = 180 \text{ Js}^{-1}\text{m}^{-2}\text{Hz}^{-1}$ at Earth, solar longitude = 300° and local time = 1 (Martian hours).

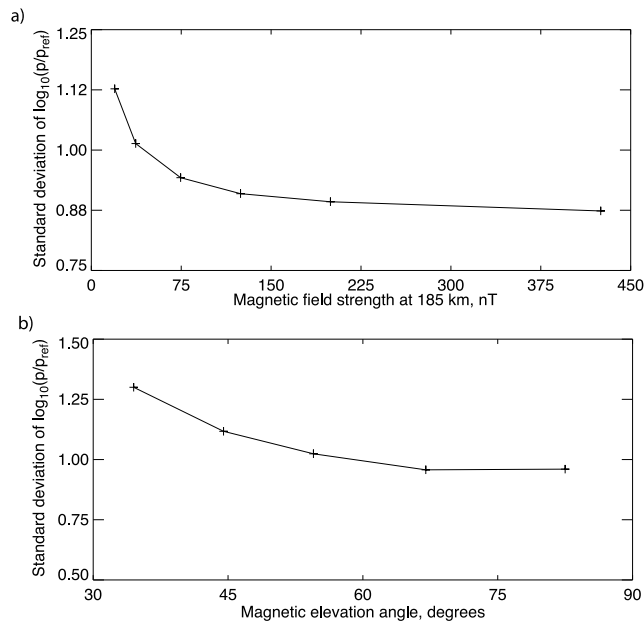


Figure 8. Standard deviation of the observed mass densities at 185 km as a function of (a) magnetic field strength at 185 km and (b) absolute magnetic elevation angle at MGS. The trends shown by the solid line are used to de-trend the data as described in the text.

peak density, equation (1) predicts smaller gradients than both of the other models. For example, the gradients in both latitude and LT are approximately half as large in the present empirical model than in the DTM-Mars model. It is reasonable to hypothesize that this difference is the result of the difference in altitude of the two model outputs, but as the empirical model presented here is not valid down to altitudes of 150 km it is not possible to establish this with any certainty.

[33] Figure 7b can be compared with the original data shown in Figure 4a, noting that 4a includes data from all LT, whereas 7b is restricted to a LT of 1. The empirical model reproduces the minimum in density around aphelion and maximum around perihelion that is seen in the original data. Comparing these two time periods, the empirical model reveals a strong latitudinal gradient at aphelion and very little asymmetry at perihelion. This feature has been reported in the temperatures of the lower thermosphere by *Bougher et al.* [2006]. Given that the density of the thermosphere at 185 km responds strongly to the temperature profile of the atmosphere below that altitudes, such a correspondence may be expected and provides reassurance that the empirical model presented here is capturing the main features of the variations in the Martian upper thermospheric density.

[34] Figure 7c can be compared with the dust opacity trends shown in Figures 6b and 6c. Both indicate an increase in the density with dust opacity at all latitudes, with the strongest response at midlatitudes. The empirical model predicts that the density increases by a factor of ~ 2 at 185 km as the dust opacity increases from 0–1. This falls in-between the factor of 3 increase in the density observed in the lower-thermosphere in response to the Noachis dust storm of 1997 reported by *Keating et al.* [1998] and the

absence of a response observed at 390 km reported by *Forbes et al.* [2008]. The closest comparison to our empirical model comes from the observations of the neutral density at 170–180 km from *Tracadas et al.* [2001]. Using Doppler tracking of the MGS spacecraft, they observed a 100% increase in density in response to a moderate dust storm, during which the dust opacity changed from 0.1–0.35. A similar increase in dust opacity level would produce an increase of $\sim 50\%$ in our empirical model, which is in reasonably good agreement with this prior observation.

5. Short-Term and Small-Scale Variability in ρ_{185}

[35] The empirical model describes the long-term and large-scale behavior of the density of the upper thermosphere. The observed value of ρ_{185} at any given time will deviate from the value predicted by the empirical model because of a combination of natural short-term and/or small-scale fluctuations in ρ_{185} and variations due to instrumental uncertainties associated with the PADs. Thus, the values of ρ_{185} that have now been de-trended for all of the large-scale and long-term variations described in section 3 represent the combination of these two sources of variation. In this section, these values will be used to investigate the behavior of the atmospheric variability as a function of latitude and season.

5.1. Instrumental Uncertainties

[36] *Lillis et al.* [2010] examined the potential sources of variability in the retrieved values of ρ_{185} associated with the MGS instrumentation and the ER technique. They demonstrated that the variability of the retrieved values of ρ_{185} was particularly large for values of the magnetic field lower than 15 nT at 185 km and when the absolute value of the magnetic elevation angle at MGS was less than 30° . These values have therefore been excluded from the database used in the present work. However, even at larger values of the field strength and elevation angle, some remnant of these apparent instrumental and/or technique related influences may still exist and must be accounted for in order to correctly find the atmospheric variability. Figure 8 shows the trend in the standard deviation of the de-trended values of ρ_{185} with (a) the magnitude of the magnetic field at 185 km and (b) the magnetic field elevation-angle at MGS. Both show some trend, with the standard deviations minimizing at larger observed field strengths and when the magnetic elevation angle approaches 90° . The trend with crustal magnetic field strength is entirely to be expected as since a weaker permanent crustal magnetic field will be more dominated by the 5–15 nT external magnetic field, whose natural variations will affect PADs in a way that mimics changes in thermospheric density. The elevation angle trend is also to be expected since the geometry of crustal magnetic cusps [*Brain et al.*, 2007] is such that open magnetic field lines tend to be more vertical where the crustal field is stronger.

[37] As these data represent the standard deviations across all data, with no substantial bias in terms of latitude, local time or season over the range of magnetic fields and elevation angles, it is reasonable to assume that these trends are inherent in the ER technique and are not of atmospheric origin. Further, if the assumption is made that the optimal situation would be a magnetic field strength of ~ 600 nT at 185 km and a magnetic elevation angle of 90° , the increase

in the standard deviations associated with observations made away from these conditions can be accounted for and removed in the following analysis, leaving values that are more representative of the natural variability of the atmosphere. This is done before any subsequent evaluation of these data.

[38] *Lillis et al.* [2010] discounted all data taken during sunlight due to potential contamination of the observed PADs by photoelectrons and the greater uncertainty regarding the magnetic field mapping. As we have removed the large-scale variations of ρ_{185} and removed contributions to the uncertainty due to the magnetic field described above, it is now possible to quantitatively assess the uncertainty in these dayside data, compared to those taken on the nightside. Such an analysis is not easy to perform in the polar regions due to seasonal variations in the availability of dayside/nightside data. If we instead limit our analysis to data taken between $\pm 66^\circ$ latitude, the globally- and seasonally-averaged standard deviation of the dayside de-trended values of ρ_{185} is only 110% of those taken in shadow. This demonstrates that by using our updated criteria, we have been able to select only those dayside data that are comparable in quality to those on the nightside and that the empirical model fits are essentially as good on the dayside as the nightside (to within $\sim 10\%$), thus justifying our inclusion of these data in the formulation of our model. Nonetheless, as we have now quantified the difference in standard deviations between the dayside and nightside residual values, we can account for this in the same manner as the magnetic field effect listed above. Finally, to further examine the dayside/nightside differences in detail, the following analyses will be performed with and without the data taken during daylight.

5.2. Natural Variability

[39] The short-term and/or small-scale variability of ρ_{185} can be defined in more than one way. First, within some range of space and time (areographic latitude and solar longitude for example), the standard deviation of the de-trended values of ρ_{185} can be found. This value would then represent the variability about the mean value associated with (1) longitudinal density changes associated with non-migrating tides (both diurnal and semi-diurnal), (2) any changes in the amplitude or phase of the migrating tides (whose long-term average behavior has been accounted for with the empirical model), (3) variations on the order of several days through inter-annual variations, (4) atmospheric gravity waves and small-scale turbulence, (5) any remaining uncertainty in ρ_{185} still associated with the observations or ER technique and (6) any stationary longitudinal variations associated with the lower levels of the atmosphere or surface. Secondly, where such observations exist, it is possible to find the change in ρ_{185} from one orbit to the next for observations made at approximately the same LT and latitude. Performing this analysis, as compared to the first analysis, removes essentially all of the contribution from factors (2) and (3) and minimizes the effect of factor (1) as the range of longitudes between the two observations is minimized. Thus, the primary sources of the variability assessed in this way may be expected to be from gravity waves, turbulence, the ER technique and any stationary longitudinal variations associated with lower levels of the atmosphere or surface. However, the assessment of the change from one orbit to the next is only

possible in regions where the distribution of observations is favorable. Examining Figure 1, it is clear that this would mean only very limited data would exist in the northern hemisphere beyond 45° latitude. Finally, to limit the impact of any influence of photoelectrons or uncertainty in the magnetic field, limiting the analysis to nighttime observations is possible. However, this would introduce significant data gaps in the polar regions around the solstices. Figure 9 shows all four permutations of the analysis of the variability of ρ_{185} described above.

[40] Examining the orbit-to-orbit differences, very little difference is seen between the day and night (Figure 9a) and the night-only plots (Figure 9b), apart from the night-only data gaps in the summer polar regions. This provides a high degree of confidence in the day-night values shown in Figure 9a, except for at latitudes north of 45° , indicated by the grayed-out area. Examining these day-night values, it can be seen that the orbit-to-orbit differences exhibit a seasonal pattern, maximizing around perihelion and minimizing around aphelion. This appears to indicate that the thermospheric density is more variable at the same time that the global mean thermospheric density is highest (Figure 4). Further, there appears to be some latitudinal variation in the orbit-to-orbit differences, which minimizes at the equator and peaks at mid to high latitudes (although this cannot be verified for high northern latitudes).

[41] Figures 9c and d show slightly more difference between the day-night and night-only values of the standard deviation of the thermospheric density than is seen in the orbit-to-orbit differences, but both Figures 9c and 9d still show the same overall seasonal and latitudinal behavior. Therefore, the day-night values will be used in the following discussion. The standard deviations show a clear seasonal variation, an increase at all latitudes just prior to perihelion and summer-winter asymmetries at each solstice, with maxima in the high-latitude summer hemispheres and minima in the high-latitude winter hemispheres. The orbit-to-orbit differences are unable to provide information about the hemispheric asymmetries, but there is good data coverage near the equator. The orbit-to-orbit differences do not appear to show the same kind of increase at the equator prior to perihelion that is seen in the standard deviations, indicating that this feature may be the result of some combination of factors 1–3 described above. Given the value of solar longitude for which this increase occurs, a likely candidate is the increased inter-annual variability associated with the large dust-storm of Mars Year 25. The effect of this dust-storm can be isolated by plotting the values of the standard deviation as a function of cumulative solar longitude over several years, as shown in Figure 10. By evaluating the standard deviations in this way, any mean shift in the density associated with the dust storm of Mars Year 25 this is not accounted for by the empirical model will not produce large values of the standard deviation.

[42] Figure 10 shows that the pattern of the standard deviations varies inter-annually, but several common features persist. The values of the standard deviation peak in the southern hemisphere around equinox and globally around perihelion. An annual minimum appears in the northern hemisphere between equinox and northern summer. With the exception of a few bins around a cumulative solar longitude of 1000° , the values of the standard deviation are all

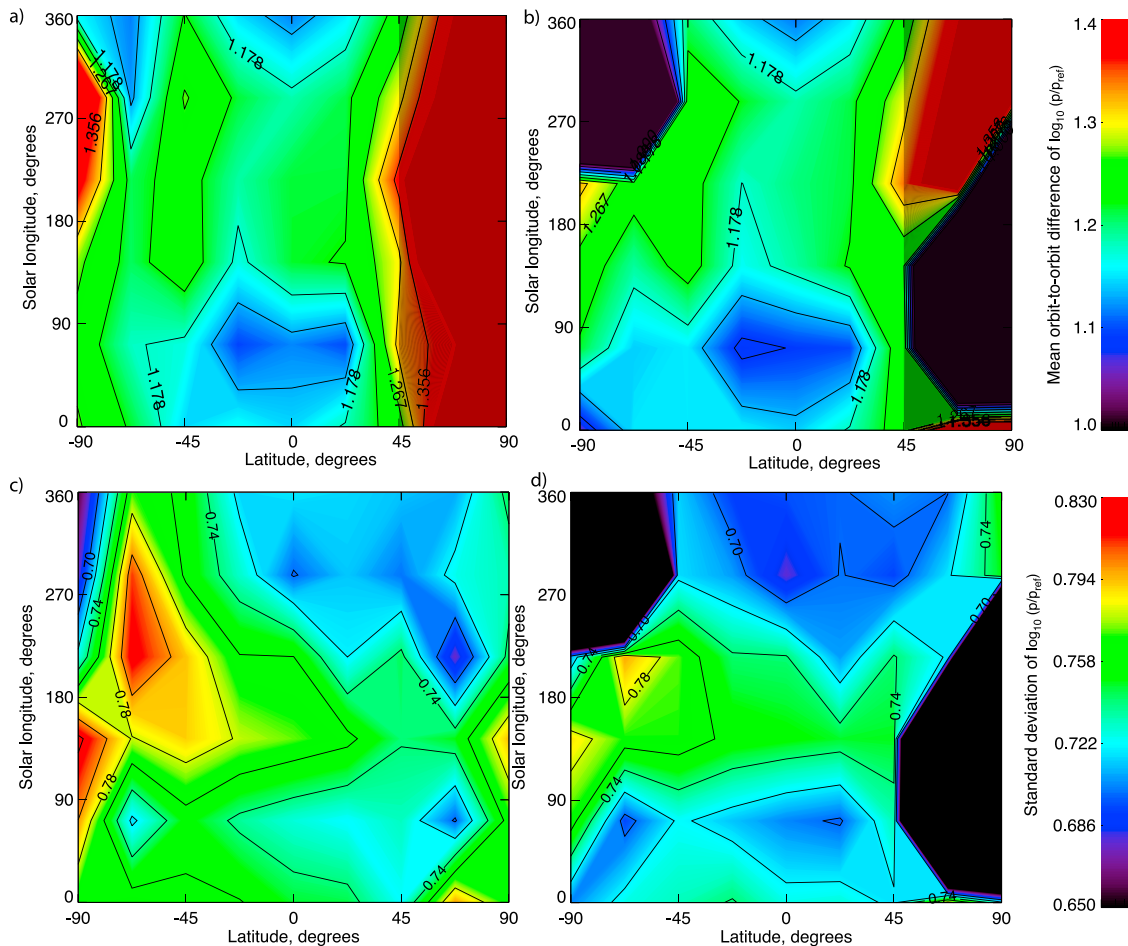


Figure 9. (a) Mean orbit-to-orbit difference in the observed mass densities at 185 km as a function of solar longitude and areographical latitude, (b) as Figure 8a but restricted to data with solar zenith angles greater than 113° , (c) as Figure 9a but showing the standard deviation of the de-trended mass densities at 185 km, and (d) as Figure 9c but restricted to data with solar zenith angles greater than 113° . Areas shaded in black show regions in which no data exist. In Figures 9a and 9b, very little data exist beyond 45° north, indicated by the grayed-out area.

larger in the southern hemisphere than the northern hemisphere. This appears to indicate that, when inter-annual variability is eliminated, the upper thermospheric density in the southern hemisphere is consistently more variable than the northern hemisphere. A similar analysis of the multiyear variations in the orbit-to-orbit differences cannot be performed as there is insufficient data to find these values.

[43] It is instructive to compare the measures of the variability of the upper thermosphere shown in Figures 9a, 9c and 10 with potential sources of this variability. The consistently higher standard deviations in the southern hemisphere shown in Figure 10 suggests that an additional source of variability may be present in the southern hemisphere. One potential candidate is the hemispheric asymmetry in Mars' topography. The distribution of topographic features is such that more stress is created as the winds flow over this topography in the southern hemisphere than in the northern hemisphere, especially poleward of 45° [Creasey *et al.*, 2006a]. This stress acts as a source of gravity waves and turbulence in the atmosphere and thus is worth considering as a source of the hemispheric asymmetry in Figure 10.

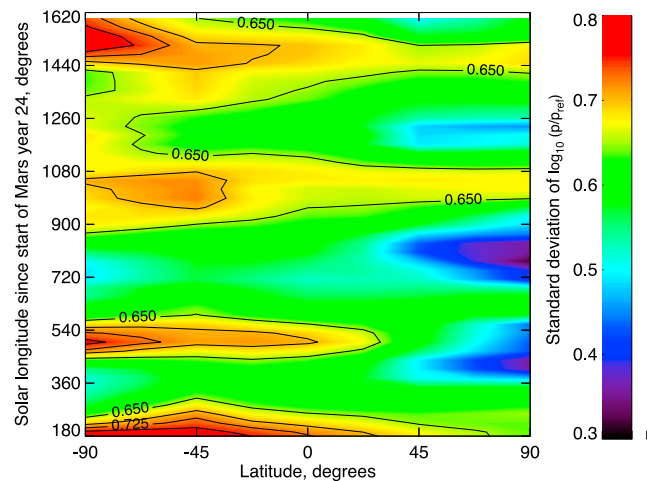


Figure 10. As Figure 9c, plotted as a function of cumulative solar longitude since the start of Mars year 24.

However, as demonstrated by *Creasey et al.* [2006a], some of the strongest wind stresses occur in the equatorial region, which is where the standard deviations generally minimize in Figure 10. Further, *Creasey et al.* [2006a] showed that this wind stress source does not correlate well with the observed short vertical wavelength gravity waves in the lower atmosphere and *Creasey et al.* [2006b] went on to show that while the equatorial region shows the highest gravity wave activity in the lower atmosphere, this region has the lowest gravity wave activity in the thermosphere. Therefore the topography of Mars appears to be an unlikely candidate for the direct cause of the hemispheric asymmetry in the standard deviations shown in Figure 10.

[44] A number of previous studies have presented observations of the distribution of gravity wave activity in the lower thermosphere, which may be a better indicator of the gravity wave distribution in the upper thermosphere, and hence more representative of their contribution to the variability demonstrated here. The main information regarding gravity waves in the lower thermosphere has come from accelerometer data taken during the aerobraking phases of the MGS, MRO and ODY missions. These are able to characterize the wavelength and amplitudes of gravity waves in the ~ 100 – 140 km altitude region. The distribution of all of the available data with respect to LT, solar longitude and latitude has been summarized by *Tolson et al.* [2007] (see their Figure 1). In the same work, the authors showed that the gravity wave amplitudes in the lower thermosphere have a high degree of spatial and temporal variability, which they attributed to filtering by large-scale waves and tides. Both *Fritts et al.* [2006] and *Creasey et al.* [2006b] have examined the latitudinal structure gravity wave amplitudes in the lower thermosphere and showed that the lowest amplitudes were observed at equatorial latitudes and the largest amplitudes were observed at high latitudes. In their observations, the highest amplitudes were observed in winter and the lowest in spring and summer. Both authors attributed this pattern to filtering of the gravity waves. However, as noted by the authors, the distribution of observations used had insufficient coverage to resolve both the latitudinal and seasonal variability simultaneously. The closest comparison to these gravity wave amplitudes that can be made using the present data set is the orbit-to-orbit differences shown in Figure 9a. These data indicate that the minimum differences are seen at the equator during all seasons, which is in agreement with the observations of *Fritts et al.* [2006] and *Creasey et al.* [2006b] and indicates that gravity waves may contribute significantly to the orbit-to-orbit differences measured here. However, the variation at midlatitudes shown in Figure 9a is highly variable with solar longitude. The observations are insufficient to examine the trend in the northern hemisphere, but in the high-latitude southern hemisphere the orbit-to-orbit differences are lower in the winter than summer, which is counter to that reported by the studies cited above. Given the seasonal-latitudinal trend shown in Figure 9a, it is clear that further observations of the gravity wave amplitudes, covering more combinations of these two parameters are needed in order to determine the actual seasonal-latitudinal trend in gravity wave amplitudes.

[45] As non-migrative tides and stationary planetary waves contribute to both of the analyses of the variability presented here, is instructive to compare these to the previous

observations of these waves in the thermosphere. *Withers et al.* [2003] examined the accelerometer data from MGS for non-migrating tides and stationary planetary waves that have zonal wave numbers of 1–4 when observed in a fixed LT frame. Of these, they found that the wave number-2 components had the largest amplitude at 130 km altitude and also the longest predicted vertical wavelengths. As dissipation processes favor the propagation of longer vertical wavelength waves over those of shorter vertical wavelengths, the waves that produce a zonal wave number of 2 maybe considered a likely candidate for the source of atmospheric variability observed at 185 km presented here. The analysis of *Withers et al.* [2003] showed that the wave number-2 components were observed to have a stronger amplitude in the southern hemisphere than the northern hemisphere (see their Figure 10), which could provide an explanation for the hemispheric asymmetry in the standard deviations presented here. *Moudden and Forbes* [2008] also examined the MGS accelerometer data for density structures with zonal wave numbers 1–3 associated with non-migrating tides and stationary planetary waves. Their analysis showed that all of these components were strong at 120 km altitude and of these, both the wave number-1 and -2 components were stronger in the southern hemisphere than the northern hemisphere and the wave number-3 component was approximately symmetric in latitude. While this does not agree in detail with the findings of *Withers et al.* [2003], these results would again support the theory that these planetary-scale waves could be the source of the hemispheric asymmetry in the standard deviations shown in Figure 10. However, as these waves have been seen to vary strongly with solar longitude [*Mazarico et al.*, 2008], observations of these waves over a full Martian year would be needed to isolate their contribution to the pattern shown in Figure 10 from the other sources described above.

6. Conclusions

[46] A new empirical model of the neutral mass density of the upper Martian thermosphere, based on the ER inversion of the MGS observations has been presented. This model reveals some of the same basic latitudinal and seasonal structure that has previously been observed in the thermosphere. The fits to the model revealed that, while the dayside neutral mass density responds to changes in solar UV flux, no response could be found on the nightside, indicating that other processes dominate the neutral mass density in the upper thermosphere at this time. This is particularly important as it has proven difficult to simulate the density of this region during the night, which may be due to the difficulty associated with simulating nightside diabatic cooling and dynamical processes. The response of the neutral density to lower-atmospheric dust opacity was shown to vary with latitude, with the strongest response seen at midlatitudes.

[47] Using the empirical model, the orbit-to-orbit differences and standard deviations of the de-trended atmospheric densities were used to investigate small-scale and short-term variations in the thermosphere. The orbit-to-orbit differences minimize at equatorial latitudes for all seasons, which is in general agreement with the latitudinal variations in gravity wave amplitudes that has been reported previously. The orbit-to-orbit differences also show a clear seasonal variation,

peaking at perihelion and minimizing around aphelion. As a result of the strength and topology of the Martian crustal magnetic fields, full latitudinal coverage of data only exist in the southern hemisphere. In this region, the orbit-to-orbit differences minimize in winter and maximize in summer, which is the opposite of the variations in gravity wave amplitudes that has been reported previously. The standard deviations reveal a strong seasonal cycle, peaking in summer in both hemispheres and showing a global increase around perihelion. The standard deviations show a degree of inter-annual variability, but show the same general annual cycle persisting over at least four Martian Years. The standard deviations also show that the southern hemisphere is consistently more variable than the northern hemisphere. Comparison to previous observations suggests that one explanation for this could be the hemispheric asymmetry in non-migrating tides. Regardless of the source of this asymmetry, the higher degree of variability of the southern hemisphere may have significant implications for studies of atmospheric escape. Both analyses of the variability of the upper thermosphere indicate that the global-maximum in variability occurs slightly before and around perihelion, when solar irradiance and solar wind pressure maximize, which may again have significant implications for studies of atmospheric escape. The results presented here also highlight the need for studies of atmospheric variability to resolve both latitudinal and seasonal effects simultaneously and hence, the need for the upcoming MAVEN observations.

[48] **Acknowledgments.** S.L.E. was supported by the Jet Propulsion Laboratory's MAVEN Critical Data Products Program, award number 1406860. R.J.L. was supported by NASA Mars Data Analysis Program grants NNX08AK94G and NNX11A187G.

References

- Angelats i Coll, M., F. Forget, M. A. López-Valverde, P. L. Read, and S. R. Lewis (2004), Upper atmosphere of Mars up to 120 km: Mars Global Surveyor accelerometer data analysis with the LMD general circulation model, *J. Geophys. Res.*, *109*, E01011, doi:10.1029/2003JE002163.
- Bougher, S., G. Keating, R. Zurek, J. Murphy, R. Haberle, J. Hollingsworth, and R. T. Clancy (1999), Mars Global Surveyor aerobraking: Atmospheric trends and model interpretation, *Adv. Space Res.*, *23*, 1887–1897, doi:10.1016/S0273-1177(99)00272-0.
- Bougher, S. W., S. Engel, D. P. Hinson, and J. R. Murphy (2004), MGS Radio Science electron density profiles: Interannual variability and implications for the Martian neutral atmosphere, *J. Geophys. Res.*, *109*, E03010, doi:10.1029/2003JE002154.
- Bougher, S. W., J. M. Bell, J. R. Murphy, M. A. Lopez-Valverde, and P. G. Withers (2006), Polar warming in the Mars thermosphere: Seasonal variations owing to changing insolation and dust distributions, *Geophys. Res. Lett.*, *33*, L02203, doi:10.1029/2005GL024059.
- Brain, D. A., R. J. Lillis, D. L. Mitchell, J. S. Halekas, and R. P. Lin (2007), Electron pitch angle distributions as indicators of magnetic field topology near Mars, *J. Geophys. Res.*, *112*, A09201, doi:10.1029/2007JA012435.
- Bruinsma, S., and F. G. Lemoine (2002), A preliminary semiempirical thermosphere model of Mars: DTM-Mars, *J. Geophys. Res.*, *107*(E10), 5085, doi:10.1029/2001JE001508.
- Conrath, B. J., J. C. Pearl, M. D. Smith, W. C. Maguire, P. R. Christensen, S. Dason, and M. S. Kaelberer (2000), Mars Global Surveyor Thermal Emission Spectrometer (TES) observations: Atmospheric temperatures during aerobraking and science phasing, *J. Geophys. Res.*, *105*, 9509–9520, doi:10.1029/1999JE001095.
- Creasey, J. E., J. M. Forbes, and D. P. Hinson (2006a), Global and seasonal distribution of gravity wave activity in Mars' lower atmosphere derived from MGS radio occultation data, *Geophys. Res. Lett.*, *33*, L01803, doi:10.1029/2005GL024037.
- Creasey, J. E., J. M. Forbes, and G. M. Keating (2006b), Density variability at scales typical of gravity waves observed in Mars' thermosphere by the MGS accelerometer, *Geophys. Res. Lett.*, *33*, L22814, doi:10.1029/2006GL027583.
- Forbes, J. M., A. F. C. Bridger, S. W. Bougher, M. E. Hagan, J. L. Hollingsworth, G. M. Keating, and J. Murphy (2002), Nonmigrating tides in the thermosphere of Mars, *J. Geophys. Res.*, *107*(E11), 5113, doi:10.1029/2001JE001582.
- Forbes, J. M., S. Bruinsma, and F. G. Lemoine (2006), Solar rotation effects on the thermospheres of Mars and Earth, *Science*, *312*, 1366–1368, doi:10.1126/science.1126389.
- Forbes, J. M., X. Zhang, S. Palo, J. Russell, C. J. Mertens, and M. Mlynczak (2008), Tidal variability in the ionospheric dynamo region, *J. Geophys. Res.*, *113*, A02310, doi:10.1029/2007JA012737.
- Forget, F., F. Montmessin, J.-L. Bertaux, F. González-Galindo, S. Lebonnois, E. Quémerais, A. Reberac, E. Dimarellis, and M. A. López-Valverde (2009), Density and temperatures of the upper Martian atmosphere measured by stellar occultations with Mars Express SPICAM, *J. Geophys. Res.*, *114*, E01004, doi:10.1029/2008JE003086.
- Fox, J. L., and A. Dalgarno (1979), Ionization, luminosity, and heating of the upper atmosphere of Mars, *J. Geophys. Res.*, *84*, 7315–7333, doi:10.1029/JA084iA12p07315.
- Fritts, D. C., L. Wang, and R. H. Tolson (2006), Mean and gravity wave structures and variability in the Mars upper atmosphere inferred from Mars Global Surveyor and Mars Odyssey aerobraking densities, *J. Geophys. Res.*, *111*, A12304, doi:10.1029/2006JA011897.
- Haberle, R. M., et al. (1999), General circulation model simulations of the Mars Pathfinder atmospheric structure investigation/meteorology data, *J. Geophys. Res.*, *104*, 8957–8974, doi:10.1029/1998JE900040.
- Joshi, M., R. Haberle, J. Hollingsworth, and D. Hinson (2000), A comparison of MGS Phase 1 aerobraking radio occultation data and the NASA Ames Mars GCM, *J. Geophys. Res.*, *105*, 17,601–17,616, doi:10.1029/1999JE001217.
- Justus, C., and B. James (2000), Mars Global Reference Atmospheric Model 2000 Version (Mars-GRAM 2000): Users Guide, *NASA Tech. Memo.*, 10279.
- Keating, G. M., et al. (1998), The structure of the upper atmosphere of Mars: In situ accelerometer measurements from Mars Global Surveyor, *Science*, *279*, 1672–+, doi:10.1126/science.279.5357.1672.
- Liemohn, M. W., et al. (2006), Numerical interpretation of high-altitude photoelectron observations, *Icarus*, *182*, 383–395, doi:10.1016/j.icarus.2005.10.036.
- Lillis, R. J., J. H. Engel, D. L. Mitchell, D. A. Brain, R. P. Lin, S. W. Bougher, and M. H. Acuña (2005), Probing upper thermospheric neutral densities at Mars using electron reflectometry, *Geophys. Res. Lett.*, *32*, L23204, doi:10.1029/2005GL024337.
- Lillis, R. J., H. V. Frey, M. Manga, D. L. Mitchell, R. P. Lin, M. H. Acuña, and S. W. Bougher (2008a), An improved crustal magnetic field map of Mars from electron reflectometry: Highland volcano magmatic history and the end of the martian dynamo, *Icarus*, *194*, 575–596, doi:10.1016/j.icarus.2007.09.032.
- Lillis, R. J., D. L. Mitchell, R. P. Lin, and M. H. Acuña (2008b), Electron reflectometry in the martian atmosphere, *Icarus*, *194*, 544–561, doi:10.1016/j.icarus.2007.09.030.
- Lillis, R. J., J. Dufek, J. E. Bleacher, and M. Manga (2009), Demagnetization of crust by magmatic intrusion near the Arsia Mons volcano: Magnetic and thermal implications for the development of the Tharsis province, Mars, *J. Volcanol. Geothermal Res.*, *185*, 123–138.
- Lillis, R. J., S. W. Bougher, F. González-Galindo, F. Forget, M. D. Smith, and P. C. Chamberlin (2010), Four Martian years of nightside upper thermospheric mass densities derived from electron reflectometry: Method extension and comparison with GCM simulations, *J. Geophys. Res.*, *115*, E07014, doi:10.1029/2009JE003529.
- López-Valverde, M. A., D. P. Edwards, M. López-Puertas, and C. Roldán (1998), Non-local thermodynamic equilibrium in general circulation models of the Martian atmosphere: 1. Effects of the local thermodynamic equilibrium approximation on thermal cooling and solar heating, *J. Geophys. Res.*, *103*, 16,799–16,812, doi:10.1029/98JE01601.
- Mazarico, E., M. T. Zuber, F. G. Lemoine, and D. E. Smith (2008), Observation of atmospheric tides in the Martian exosphere using Mars Reconnaissance Orbiter radio tracking data, *Geophys. Res. Lett.*, *35*, L09202, doi:10.1029/2008GL033388.
- McDunn, T. L., S. W. Bougher, J. Murphy, M. D. Smith, F. Forget, J.-L. Bertaux, and F. Montmessin (2010), Simulating the density and thermal structure of the middle atmosphere (~70–130 km) of Mars using the MGCM-MTGC: A comparison with MEX/SPICAM observations, *Icarus*, *206*, 5–17, doi:10.1016/j.icarus.2009.06.034.
- Mitchell, D. L., R. P. Lin, H. Rème, D. H. Crider, P. A. Cloutier, J. E. P. Connerney, M. H. Acuña, and N. F. Ness (2000), Oxygen Auger electrons observed in Mars' ionosphere, *Geophys. Res. Lett.*, *27*, 1871–1874, doi:10.1029/1999GL010754.

- Moudden, Y., and J. M. Forbes (2008), Topographic connections with density waves in Mars' aerobraking regime, *J. Geophys. Res.*, *113*, E11009, doi:10.1029/2008JE003107.
- Smith, M. D. (2004), Interannual variability in TES atmospheric observations of Mars during 1999–2003, *Icarus*, *167*, 148–165, doi:10.1016/j.icarus.2003.09.010.
- Tolson, R., A. M. Dwyer, P. E. Escalera, B. E. George, J. L. Hanna, G. M. Keating, and M. R. Werner (2005), Application of Accelerometer Data to Mars Odyssey Aerobraking and Atmospheric Modeling, *J. Spacecraft Rockets*, *42*, 435–443, doi:10.2514/1.15173.
- Tolson, R., et al. (2008), Atmospheric modeling using accelerometer data during Mars Reconnaissance Orbiter aerobraking operations, *J. Spacecraft Rockets*, *45*, 511–518, doi:10.2514/1.34301.
- Tolson, R. H., G. M. Keating, R. W. Zurek, S. W. Bougher, C. G. Justus, and D. C. Fritts (2007), Application of accelerometer data to atmospheric modeling during Mars aerobraking operations, *J. Spacecraft Rockets*, *44*, 1172–1179, doi:10.2514/1.28472.
- Tracadas, P. W., M. T. Zuber, D. E. Smith, and F. G. Lemoine (2001), Density structure of the upper thermosphere of Mars from measurements of air drag on the Mars Global Surveyor spacecraft, *J. Geophys. Res.*, *106*, 23,349–23,358, doi:10.1029/2000JE001418.
- Wang, L., D. C. Fritts, and R. H. Tolson (2006), Nonmigrating tides inferred from the Mars Odyssey and Mars Global Surveyor aerobraking data, *Geophys. Res. Lett.*, *33*, L23201, doi:10.1029/2006GL027753.
- Wilson, R. J. (2002), Evidence for nonmigrating thermal tides in the Mars upper atmosphere from the Mars Global Surveyor accelerometer experiment, *Geophys. Res. Lett.*, *29*(7), 1120, doi:10.1029/2001GL013975.
- Withers, P. (2006), Mars Global Surveyor and Mars Odyssey Accelerometer observations of the Martian upper atmosphere during aerobraking, *Geophys. Res. Lett.*, *33*, L02201, doi:10.1029/2005GL024447.
- Withers, P., S. W. Bougher, and G. M. Keating (2003), The effects of topographically-controlled thermal tides in the martian upper atmosphere as seen by the MGS accelerometer, *Icarus*, *164*, 14–32, doi:10.1016/S0019-1035(03)00135-0.
-
- S. L. England and R. J. Lillis, Space Sciences Laboratory, University of California Berkeley, Berkeley, CA 94720, USA. (england@ssl.berkeley.edu)